Acta Astronautica 219 (2024) 318–328

Contents lists available at ScienceDirect

Acta Astronautica

journal homepage: www.elsevier.com/locate/actaastro

Research paper

# Mission analysis of a 1U CubeSat post-mission disposal using a thin-film vacuum arc thruster

Kash Saddul [*,1], James Saletes[1], Minkwan Kim[2], Alexander Wittig[2]

*Department of Aeronautics and Astronautics, University of Southampton, University Road, Southampton, SO17 1BJ, Hampshire, United Kingdom*

ARTICLE INFO

*Keywords:*
CubeSat
End-of-life de-orbiting
Electric micro-propulsion
Orbit-attitude simulations
Vacuum arc thruster

ABSTRACT

We present the operation of the CubeSat De-orbiting All-Printed Propulsion System (Cube-de-ALPS), a thin-film Vacuum Arc Thruster being developed at the University of Southampton in collaboration with the European Space Agency to provide robust de-orbiting capability to sub-3U CubeSats. It comprises a flexible substrate on which coplanar arrays of vacuum arc micro-thrusters (micro-VAT) are printed alongside small supporting electronic subsystems. In particular, we focus on the application of a Cube-de-ALPS End-Of-Life disposal to an under-actuated 1U CubeSat with uncontrolled spin. In this scenario, a Faraday cup will provide coarse angle-of-attack estimates and trigger a single micro-VAT to ignite every time it points towards the forward velocity vector. Orbital lifetime estimates for different fuel materials, configurations, and operational modes are estimated using simplified dynamics and analytical thrust averaging. These results are compared to high-fidelity numerical simulations including full six degrees of freedom coupled attitude and orbital dynamics to confirm the viability of the concept and confirm that Cube-de-ALPS can de-orbit CubeSats from 1400 km.

## 1. Introduction

In 2018, the first successful demonstration of an electric propulsion system onboard a 1U CubeSat was launched on the UWE-4 satellite [1]. This was the first and only propulsion system that could provide all CubeSats classes, down to a 1U, with greatly needed orbital manoeuvrability [2]. Indeed, between November 2005 and June 2014, each CubeSat experienced on average 2229 sub-5 km conjunctions [3]. Since then, the CubeSat population has grown significantly, and with the Spaceworks forecast predicting between 1800 and 2500 CubeSat launches between 2020 and 2025 [4,5], the number of conjunction will likely increase. The growth of the CubeSat population affects not only their collision risk but also the space environment as a whole. With 25% of all CubeSat launches ending up in a non-responsive spacecraft, CubeSats contribute to the surge in space debris [6]. The high failure rate and the IADC's de-orbiting recommendation have led many CubeSats to be limited to low orbital altitudes to guarantee passive re-entry if the satellite is dead-on-arrival [7]. However, this passive decay also restricts the lifetime of functioning satellites, which might de-orbit despite being operational [8].

While an active thruster would allow a CubeSat to operate longer and at higher altitudes, the vast majority of CubeSats (>95%) are in the Sub-3U (≤3U) range [9], meaning that their mass, volume, and power budgets are severely restricted and do not currently allow for the use of propulsion systems.

Chemical propulsion systems are of limited use on CubeSats, as the CubeSat standard limits onboard chemical energy to 100 Wh [10], equivalent to 19 g of hydrazine [2]. In addition, the typical costs associated with rigorous testing of complex propulsion systems are generally prohibitive to the smaller range of CubeSats.

Electric Propulsion (EP) systems are particularly interesting for CubeSats, as they typically present high fuel efficiency [11], leading to a smaller amount of fuel required, which could save mass and volume on the spacecraft. However, their implementation is not straightforward, as EP systems tend to come with heavy electronic components and high power requirements [12]. For example, NASA's state-of-the-art report on Gridded Ion Thrusters (GITs) [13] for small satellites lists seven GITs, with only one that could be fitted on a 1U, the Ariane Group RIT $\mu$X. Indeed, the other GITs presented in the report have a mass greater than 1.33 kg, the maximum weight of a typical 1U CubeSat [10]. The Ariane Group RIT $\mu$X is also the least power-consuming of all the GITs shown and typically uses up to 50 W of power. However, 1U CubeSats typically cannot generate more than 2 W of power, and 3U can generally produce up to 28 W, assuming highly efficient solar panels on all six faces [14,15]. This power constraint

* Corresponding author.
*E-mail address:* kash.saddul@soton.ac.uk (K. Saddul).
[1] PhD candidate.
[2] Associate Professor.

https://doi.org/10.1016/j.actaastro.2024.03.019
Received 13 October 2023; Received in revised form 11 December 2023; Accepted 13 March 2024
Available online 15 March 2024

means that current GITs are unlikely to be used on the smaller range of CubeSats, as they meet neither the mass, volume or power budget required.

Hall Effect Thrusters (HETs) are an alternative to GITs, which also have more flight heritage on CubeSats [16]. While the average system is lighter than a typical GIT, as they use magnets instead of grids, the state-of-the-art of HETs for small satellite shows that they tend to be more power intensive than the GITs, with the lowest power requirement being at 53 W [13]. Again, this proves to be unfeasible for CubeSats of the ≤3U class.

Electrospray thrusters are a form of EP suitable for the smaller end of CubeSats [17], as some have low mass, volume, and power requirements. For example, the Accion Systems TILE-2 Electrospray thruster weighs 0.45 kg and requires roughly 4 W of power [13]. As it takes only 0.5U in volume, a 3U CubeSat could potentially incorporate it as an actuator. However, the mass and power requirements are still unfeasible for smaller CubeSats. To cater for Sub-3U, one could look at the NanoFEEP thruster, which was flown on the UWE-4 satellite [1].

However, none of these options are likely to be used on such limited CubeSats, as attitude control systems are typically required to ensure the correct alignment of the thrusters [18]. This requirement for attitude control typically means that the mass, volume, and power budget must also include attitude actuators besides the mission payload.

A lightweight, low-power system is thus required to allow Sub-3U CubeSats to use active propulsion without significantly sacrificing their mission objectives. Natural candidates are Pulsed Plasma Thrusters (PPTs) and Vacuum Arc Thrusters (VATs) [2,16]. Both systems generate an electric arc across the surface of a solid propellant to vaporise and ionise it, with PPTs using Teflon and VATs using metallic propellants. Their simple design and power requirements, as low as 0.3 W [19,20], make them very suitable for both orbital and attitude control of smaller CubeSats [21].

This work uses a fully printed VAT system capable of meeting the exacting requirements of sub-3U CubeSats [22,23]. We develop the thruster system into a failsafe de-orbiting package in Section 2 and show the required components for correct operation. We subsequently apply the system to HUMSAT-D, a 1U CubeSat that was lost in 2014, one year after its launch, and accidentally re-contacted by amateur radio operators seven years later [24]. The CubeSat is in a 617 km Sun-Synchronous Orbit (SSO), one of the most crowded regions of the Low Earth Orbit (LEO) environment, highlighting the need for a de-orbiting system. Section 4 shows the thruster's performance with different fuel materials, setups and operational modes, which we validate in Section 6 with high-fidelity simulations coupling both orbital and attitude motion.

## 2. The CubeSat de-orbiting all-printed propulsion system

As part of ESA's Innovative Propulsion System for CubeSats and MicroSats, a thin-film VAT has been developed at the University of Southampton [22]. It is a fully-printed, flat system that can be placed on one or multiple sides of a 1U CubeSat and will provide thrusting capabilities. The thruster system consists of multiple arrays of micro-Vacuum Arc Thrusters (micro-VATs) that can generate, one at a time, a thrust level in the micro-Newtons using 1.5 W of power. Nominally, it is arranged in a 10 × 10 grid to provide 100 micro-VATs, and its theoretical fuel capacity provides it with one year of firing time. The developed system is aimed to fit within a 0.2U volume and weighs up to 250 g including up to 100 g of propellant. A prototype of the system, taken from [23], is shown in Fig. 1(a).

In this work, we specialise the thruster package into the CubeSat De-orbiting All-Printed Propulsion System (Cube-de-ALPS), a system designed to provide post-mission disposal capacities to sub-3U CubeSats. The system operates under the assumption that the host CubeSat is under-actuated and that Cube-de-ALPS does not control its pointing. Thus, Cube-de-ALPS will fire whenever its micro-thrusters point anywhere in the velocity direction, which relaxes the need for precise attitude determination and control. In addition to the VAT, Cube-de-ALPS includes all required attitude-sensing devices, as well as a control law for disposal and attitude maintenance.

### 2.1. Design of Cube-de-ALPS

A distinguishable feature of Cube-de-ALPS is its use of distributed propulsion architecture. Fig. 1(a) shows that Cube-de-ALPS provides multiple micro-thrusters laid out in a co-planar fashion. Each micro-thruster, also called thruster pixel, is an individual micro-VAT capable of delivering thrust. The printed VAT has re-ignitable micro-thrusters with a radius of 3 mm. To ensure total erosion of the fuel, the maximum distance between the anode and the cathode should be no greater than 4.7 mm, thus also limiting the pixel height to 3.6 mm, as shown in Fig. 1(b).

The nature of the layout leads most pixels to generate a torque upon firing as they are not aligned with the centre of mass. To counter this effect, Cube-de-ALPS divides itself into four individually addressable quadrants, as shown in Fig. 2. The four zones were chosen over individual pixel control to provide essential attitude control while keeping the electronics design simple. Cube-de-ALPS, based on its angular velocity, can decide in which quadrant a pixel will ignite, and based on the path of least electrical resistance within the quadrant's circuit, one of the micro-VATs will ignite. This selection process means Cube-de-ALPS has no control over which exact pixel will fire. Instead, it can only control in which quadrant a thruster pixel will turn on. Whenever a pixel ignites, it receives a pulsed electrical signal. At each pulse, the micro-VAT will generate a potentially widely different level thrust, according to a thrust distribution function. However, with a pulse frequency of 100 Hz, the average thrust is still closely distributed around the nominal thrust level of each pulse, as per the Central Limit Theorem [25], leading to a very consistent average thrust delivered.

Due to its printed nature, Cube-de-ALPS has inherent flexibility in its pixel layout. In this work, we study two different layouts: one Cube-de-ALPS system fitted on a single face (1-F) and another Cube-de-ALPS system split across two opposite faces (2-F) while retaining the same amount of fuel. As all faces equipped with Cube-de-ALPS also have their own Faraday cup, the 2-F layout is expected to fire more often and thus have improved de-orbiting performance.

### 2.2. On-board attitude determination

Beyond the printed VAT, Cube-de-ALPS also includes sensors to estimate its angle-of-attack and angular velocity. We introduce in this section a MEMS gyroscope that can provide accurate angular velocity readings over a long operational time, and a Faraday cup that can provide coarse angle-of-attack estimates.

*Gyroscopes for angular rates measurements*

To correctly select which quadrant to fire, Cube-de-ALPS requires knowledge of the CubeSat's angular velocity. We utilise a gyroscope to provide angular rate readings. While many gyroscopes can provide accurate angular velocity measurements, the mass and volume restrictions on Cube-de-ALPS limit the range of options. As the sensor is expected to operate for at least the nominal lifetime of Cube-de-ALPS, the thruster requires a gyroscope that produces low noise over extended periods of time. Therefore, the STIM277H, an aerospace-grade 3-axis MEMS sensor manufactured by Safran, was selected for use on Cube-de-ALPS [26]. The sensor, measuring 21.5 × 38.6 × 35.9 mm, provides readings with a standard deviation of 0.47 $\frac{\text{deg}}{\text{s}}$ after one year, which is the nominal operational lifetime. In contrast, the MP6050 MEMS gyroscope, a typical consumer-grade sensor commonly used by hobbyists, will have readings with a standard deviation of 6.7 $\frac{\text{deg}}{\text{s}}$ after one year.

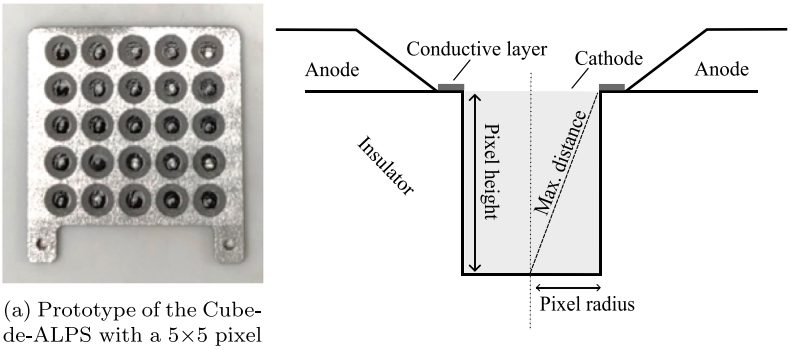


(a) Prototype of the Cube-de-ALPS with a 5×5 pixel grid.

(b) Cross-section of a pixel.

**Fig. 1.** Picture of a Cube-de-ALPS prototype and a pixel cross-section.
*Source:* Images taken and adapted from [23].

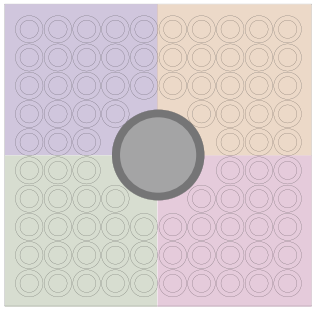

**Fig. 2.** Drawing of the thruster pixels of Cube-de-ALPS, with a Faraday cup in the centre. The different colours correspond to the quadrant division. (For interpretation of the references to color in this figure legend, the reader is referred to the web version of this article.)

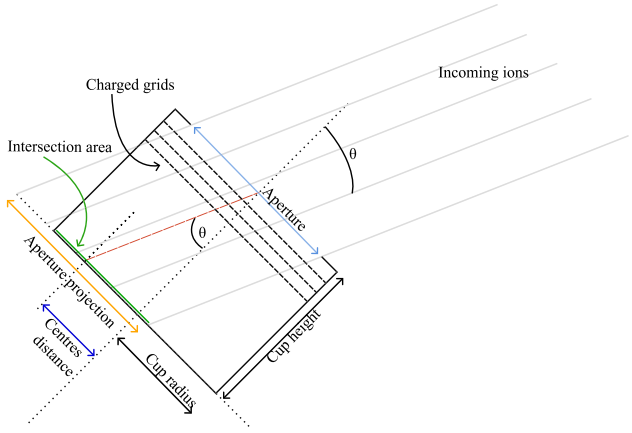


**Fig. 3.** Sketch of the Faraday cup.

*Angle-of-attack estimation with a Faraday cup*

Cube-de-ALPS must know where its pixels are pointing to provide correct de-orbiting. While commercially available solutions for attitude determination exist, with typical packages using a combination of sensors to provide accurate pointing data, these systems also tend to be voluminous and heavy [27], making them unsuitable for the Cube-de-ALPS package.

Due to the opportunistic firing law, the system requires only knowledge of its angle relative to the velocity vector, referred to as the angle-of-attack. The work of Watanabe et al. [28] shows how a Faraday cup can estimate the CubeSat's orientation relative to the velocity vector by detecting the ions from the incoming flow direction. The EGG spacecraft, a 3U CubeSat, has flown with a Faraday cup as an attitude sensor demonstrating its feasibility [29]. This method of estimating the attitude presents the advantage of being small and easy to fit on CubeSats, as the sensor is 30 mm in diameter and 10 mm in height, with an aperture of 7 mm.

The sensor detects the current generated by ions colliding with a collector plate placed behind the aperture of the Faraday cup. A series of charged grids, in-between the plate and the aperture, ensure that only ions with a high relative velocity, i.e., the spacecraft's orbital velocity, can enter the sensor. This gives confidence that a current will only be detected when facing the incoming flow. However, the detected current is proportional to the number of ions hitting the plate, given by

$$I = q_e \rho_{ions}(h) A_{fc}(\theta) v_{sc} \tag{1}$$

where $q_e$, $\rho_{ions}(h)$, $v_{sc}$ are the charge of an electron, the local density of positively charged ions as a function of altitude $h$, taken from [30], and the orbital velocity of the spacecraft, respectively. The angle-of-attack $\theta$ is measured between the flow direction and the Faraday cup centreline, and the variable $A_{fc}(\theta)$ denotes the area of the collector plate that ions can hit, shown in Fig. 3 as the intersection area. As the spacecraft velocity is significantly higher than the thermal velocity of the ions [31], we model the incoming flow as parallel rays that project the aperture on the collector plate plane at a distance $d$ from the sensor centreline,

$$d(\theta) = h_{fc} \tan(\theta) \tag{2}$$

where $h_{fc}$ is the height of the Faraday cup. The overlapping area between the sensor and the projected aperture corresponds to $A_{fc}(\theta)$ and is computed as the intersection area between two circles of equal radius $r_{fc}$ [32],

$$A_{fc} = 2r_{fc}^2 \arcsin\left(\frac{\sqrt{r_{fc}^2 - \frac{d^2(\theta)}{4}}}{r_{fc}}\right) - d(\theta)\sqrt{r_{fc}^2 - \frac{d^2(\theta)}{4}}. \tag{3}$$

The Faraday cup on the EGG spacecraft has flown at altitudes lower than 500 km, where positive oxygen ions are present at a density of $10^5$ ions cm$^{-3}$ [33]. The work of Nanan et al. [30] shows that while the density of positive Oxygen ions lowers above 500 km, the number of protons ($H^+$) increases and stagnates at $10^4$ ions cm$^{-3}$, up to at least 2000 km. We ensure operation at higher altitudes by increasing the aperture of the Faraday cup to the collector plate diameter. As no other design parameters need to be changed, the sensor remains at the same dimensions, which leads to 12 pixels being removed from the Cube-de-ALPS grid, as shown in Fig. 2. Due to the presence of thruster pixels in proximity to the Faraday cup, contamination from the plume is a potential concern. However, due to the presence of the charged

**Table 1**
Summary of Cube-de-ALPS sensors and properties.

| Property | Value |
|---|---|
| Max. pixel height [mm] | 3.6 |
| Max. fuel mass [g] | 100 |
| Max. total system mass [g] | 250 |
| Max. system volume [U] | 0.2 |
| Operational power [W] | 1.5 |
| Pulse standard deviation [%] | 10 |
| Pulse frequency [Hz] | 100 |
| Number of pixels [–] | 88 |
| Number of quadrants [–] | 4 |
| Gyroscope | STIM277H |
| Faraday cup dimensions [mm] | 30 × 10 |

grids, which allow only high velocity ions to enter the Faraday cup, we believe that this is not an issue.

With the addition of the Faraday cup and the gyroscope, Cube-de-ALPS can now estimate its angle-of-attack and angular velocity. Table 1 provides a summary of the sensors, the characteristics and constraints of Cube-de-ALPS assumed for the simulations carried out in this work.

### 2.3. On-board firing criterion

Cube-de-ALPS is assumed to turn on at the end of the mission life of the host CubeSat or shortly after launcher separation if the spacecraft is dead-on-arrival.

To ensure de-orbiting, the system must thrust to slow down the orbital velocity of the host CubeSat, which can be achieved by firing against the velocity direction. Because the measurements of the Faraday cup are electrical current readings, the exact angle-of-attack $\theta$ of the spacecraft cannot be determined onboard. Indeed, solving Eq. (1) for $\theta$ would require knowledge of the spacecraft's velocity and altitude. However, Cube-de-ALPS cannot obtain real-time orbital height and velocity measurements.

Fortunately, the exact angle is not required to determine whether the Faraday cup is facing forward. Instead, the system can decide to fire whenever it detects a signal above its expected noise $\epsilon$, which would imply that it is facing the incoming flow. This mode of operation consists of firing when the signal-to-noise ratio $SN$ is equal to or above a given value. It can be expressed as

$$SN = \frac{q_e}{\epsilon}\rho_{ions}(h)A_{fc}(\theta)v_{sc} \tag{4}$$

and the firing criterion is

$$SN \geq SN_{firing} \tag{5}$$

where $SN_{firing}$ is the desired minimal signal-to-noise ratio.

Eq. (4) shows that the signal detected varies with the angle-of-attack, and a brief investigation of Fig. 3 indicates that as $\theta$ increases, the signal will decrease to zero. Therefore, there must exist an angle $\alpha$ where the signal detected is equal to our firing criterion,

$$SN(\alpha) = SN_{firing}. \tag{6}$$

We call the cone defined by the half-angle $\alpha$ the thrusting cone, which is the region where $SN \geq SN_{firing}$. Due to the variation of ion density with altitude, the thrusting cone half-angle is a function of orbital height, which varies in time.

If the firing criterion in Eq. (5) is true, by definition, the Faraday cup must be inside the thrusting cone, so Eq. (5) is equivalent to

$$\theta \leq \alpha(h(t), SN_{firing}) \tag{7}$$

where the value of $SN_{firing}$ will determine the profile of $\alpha$ with respect to altitude. This criterion is not usable onboard the CubeSat but is useful to understand the thrusting profile of Cube-de-ALPS. Generally, a higher $SN_{firing}$ means the thrusting cone is smaller throughout all altitudes compared to a lower signal-to-noise ratio. Similarly, the thrusting cone $\alpha$ is smaller at higher altitudes and combinations of high $SN_{firing}$ and high altitudes can even make it disappear, in which case Cube-de-ALPS does not fire in any direction.

## 3. Semi-analytical model

A custom simulation environment was created to model the effect of Cube-de-ALPS on the orbital evolution of CubeSats. It includes the perturbations from the space environment and the thrust from Cube-de-ALPS. The orbital parameters are expressed in modified equinoctial elements to avoid singularities at polar, circular and equatorial orbits. Their evolution under the effect of external perturbations is given by the Gauss equations [34]:

$$\frac{dp}{dt} = \frac{2p}{w}\sqrt{\frac{p}{\mu}}a_t \tag{8}$$

$$\frac{df}{dt} = \sqrt{\frac{p}{\mu}}\left(a_r\sin(L) + ((w+1)\cos(L)+f)\frac{a_t}{w} - (h_{eq}\sin(L) - k\cos(L))\frac{g}{w}a_w\right) \tag{9}$$

$$\frac{dg}{dt} = \sqrt{\frac{p}{\mu}}\left(-a_r\cos(L) + ((w+1)\sin(L)+g)\frac{a_t}{w} + (h_{eq}\sin(L) - k\cos(L))\frac{f}{w}a_w\right) \tag{10}$$

$$\frac{dh_{eq}}{dt} = \sqrt{\frac{p}{\mu}}\frac{s^2 a_w}{2w}\cos(L) \tag{11}$$

$$\frac{dk}{dt} = \sqrt{\frac{p}{\mu}}\frac{s^2 a_w}{2w}\sin(L) \tag{12}$$

$$\frac{dL}{dt} = \sqrt{\mu p}\left(\frac{w}{p}\right)^2 + \frac{1}{w}\sqrt{\frac{p}{\mu}}(h_{eq}\sin(L) - k\cos(L))a_w \tag{13}$$

with the values

$$w = 1 + f\cos(L) + g\sin(L) \tag{14}$$

$$\alpha = \sqrt{h_{eq}^2 - k^2} \tag{15}$$

$$s = \sqrt{1 + h_{eq}^2 + k^2} \tag{16}$$

$$r = \frac{p}{w} \tag{17}$$

Accurately modelling the thrust effects requires knowledge of Cube-de-ALPS's orientation. However, this can be computationally expensive and difficult to achieve. Thus, we initially ignore the propagation of the attitude and analytically average the thrust while propagating the orbital motion numerically, forming a semi-analytical propagator. This section will describe the perturbation models used for the orbital motion and detail the averaging technique used for the thrust. The semi-analytical model trades accuracy for performance, ignoring the accurate attitude motion, the actual thrust direction and the impact of the thrust on the attitude, but typically allows simulation of 90 years of orbital evolution in approximately 10 h using a non-optimised Python code on a desktop machine.

### 3.1. Aerodynamic forces

We compute the drag using

$$\vec{a}_{Drag} = -\frac{1}{2}\frac{C_D A_{\hat{v}}}{m}\rho\left(h, T_{unc}\right)v_{rel}^2\frac{\vec{v}_{rel}}{\|\vec{v}_{rel}\|} \tag{18}$$

where $m$ is the CubeSat's mass, $C_D$ is the drag coefficient, $A_{\hat{v}}$ is the projected area towards the velocity direction, and $v_{rel}$ is the relative velocity between the spacecraft and the rotating atmosphere. The simulation environment computes the atmospheric density $\rho(h, T_{unc})$ through an interpolation of the Jacchia-77 atmospheric model introduced in Frey and Colombo [35], which allows for both static and temperature-dependent models. We represent a dynamic atmosphere using the uncorrected exospheric temperature $T_{unc}$ to compute the density at a given position and time [36].

### 3.2. Geopotential perturbations

To model the non-spherical shape of the Earth, the gravity potential is modelled with spherical harmonics [36]. We use the Earth Gravity Model 2008 (EGM08) to determine the harmonic expansion coefficients [37]. For simplicity, we use a Python wrapper [38] of the NAIF SPICE software [39,40] to compute the Earth's orientation at any given time.

### 3.3. Solar radiation pressure

We model the solar radiation pressure (SRP) for increased fidelity in the simulations, with

$$\vec{a}_{srp} = \sigma P_{Sun} \frac{C_R A_{\hat{s}}}{m_{sat}} \frac{\vec{r}_{sun-sat}}{r_{sun-sat}} \tag{19}$$

where $P_{Sun}$ is the solar pressure at the satellite position, $C_R$ is the reflection coefficient, $A_{\hat{s}}$ is the projected area towards the sun, $m_{sat}$ is the mass of the satellite, and $\vec{r}_{sun-sat}$ is the vector from the sun to the satellite.

The fraction of the solar disk visible from the satellite's position is denoted as $\sigma$ [41,42].

### 3.4. Sun and Moon gravitational effect

We model the gravitational influence of the Sun and the Moon with

$$\vec{a}_{Luni-Solar} = Gm_L \left( \frac{\vec{r}_{L-sat}}{r^3_{L-sat}} - \frac{\vec{r}_{E-L}}{r^3_{E-L}} \right) + Gm_{sun} \left( \frac{\vec{r}_{sun-sat}}{r^3_{sun-sat}} - \frac{\vec{r}_{E-sun}}{r^3_{E-sun}} \right) \tag{20}$$

where $Gm_L$ and $Gm_{sun}$ are the gravitational parameters of the Moon and Sun, respectively. The vectors $\vec{r}_{E-L}$ and $\vec{r}_{E-sun}$ are the positions of the Moon and the Sun in the Earth Centered Inertial (ECI) frame, which we obtain from the NAIF SPICE library using the "de440.bsp" kernel [43], and allow the computation of $\vec{r}_{L-sat}$ and $\vec{r}_{sun-sat}$, which are the Moon-satellite and Sun-satellite vectors in the same frame.

### 3.5. Thrust averaging

Given a Cube-de-ALPS configuration with a fixed amount of fuel, or equivalently a total firing time $t_{firing}$, we model the thrust as a constant average thrust $\hat{T}_{eff}$ along the velocity direction throughout the mission duration.

To obtain $\hat{T}_{eff}$, the thrust delivered along the velocity direction throughout the entire mission is averaged analytically, while the effect of transversal thrust is ignored. We assume a random, uncontrolled tumbling of the spacecraft, making it equally likely to point in any direction relative to the orbital velocity vector. As CubeSats generally do not have actuation systems [44], this assumption seems reasonable, although passive stabilisation methods, such as hysteresis rods or deployables for aerodynamic stabilisation, could affect this assumption based on the CubeSat's altitude [45,46].

We start by defining a coordinate system centred on the spacecraft with its $\hat{z}$ axis aligned with the orbital velocity direction $\hat{v}$, as represented in Fig. 4. The angle $\alpha$ denotes the half-angle of the thrusting cone around the velocity direction. The highlighted sphere cap enclosed by the thrusting cone indicates all spacecraft orientations in which Cube-de-ALPS fires.

Since we assume all orientations to be equally likely over time, the fraction of time the system is thrusting, $\tau_t$, is the same as the fraction of the surface of the full unit sphere covered by the sphere cap [47]:

$$\tau_t = \frac{A_{cap}}{A_{sphere}} = \frac{2\pi\,(1-\cos(\alpha))}{4\pi} = \frac{1-\cos(\alpha)}{2}. \tag{21}$$

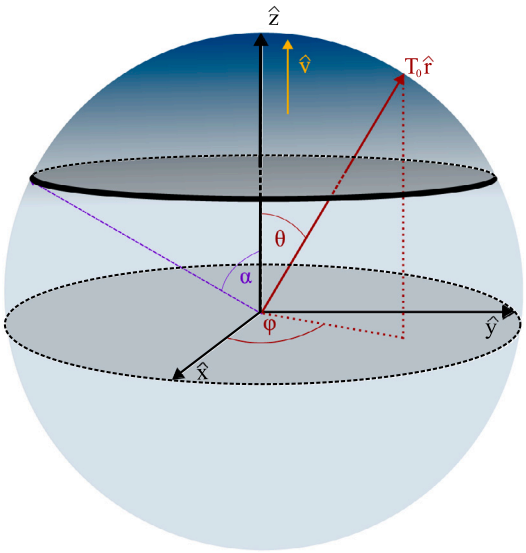


**Fig. 4.** Unit sphere of all possible spacecraft orientations with the thrusting cone defined by $\alpha$. The highlighted sphere cap enclosed by the thrusting cone indicates all orientations in which Cube-de-ALPS fires.

Similarly, we can calculate the average thrust delivered in the velocity direction when the system is thrusting by averaging the projection of the thrust on $\hat{v}$ over the sphere cap:

$$\begin{aligned} \hat{T}_\alpha &= \frac{T_0}{A_{cap}} \int_{cap} \hat{r} \cdot \hat{v}\; dA \\ &= \frac{T_0}{2\pi\,(1-\cos(\alpha))} \int_0^{2\pi} \int_0^{\alpha} \cos(\theta)\;\sin(\theta) d\theta d\phi \\ &= T_0 \left( \frac{1+\cos(\alpha)}{2} \right) \end{aligned} \tag{22}$$

where $T_0\hat{r}$ is the thrust vector. Knowing the nominal firing time $t_{firing}$ and $\tau_t$ we can calculate the total mission duration throughout which Cube-de-ALPS is operational as

$$t_{mission} = \frac{t_{firing}}{\tau_t}. \tag{23}$$

We can also obtain the total impulse imparted in the velocity direction throughout the mission as

$$I_{\hat{v}} = \hat{T}_\alpha t_{firing}. \tag{24}$$

Finally, to obtain the equivalent average thrust $\hat{T}_{eff}$ constantly acting along the velocity direction throughout the entire mission duration $t_{mission}$ and delivering the same total impulse $I_{\hat{v}}$, we define

$$\hat{T}_{eff} = \frac{I_{\hat{v}}}{t_{mission}} = \tau_t \hat{T}_\alpha = T_0 \left( \frac{1-\cos^2(\alpha)}{4} \right) \tag{25}$$

An important relationship between $\alpha$, $\hat{T}_{eff}$, and $I_{\hat{v}}$ emerges out of Eqs. (24) and (25): An increased cone size $\alpha$ also increases the effective thrust, but leads to a loss on the total impulse delivered against the velocity direction. This is because a bigger thrusting cone half-angle $\alpha$ means Cube-de-ALPS can fire more often, but it will also thrust less accurately with a lower average component of thrust aligned in the desired direction.

If we consider the case where Cube-de-ALPS is split across two opposite faces, then the 2-F layout can fire twice as often as the 1-F setup, which leads Eq. (21) to become

$$\tau_{t,2F} = 1 - \cos(\alpha). \tag{26}$$

Splitting the layout between two faces does not affect $\hat{T}_\alpha$, and the new effective thrust can be computed using (25)

$$\hat{T}_{eff,2F} = \tau_{t,2F} \hat{T}_\alpha = 2\hat{T}_{eff,1F}. \tag{27}$$

**Table 2**
HUMSAT-D satellite properties.

| Property | Value |
|---|---|
| Orbit inclination [deg] | 97.8 |
| Start date [–] | 1 Dec 2014 |
| Fixed projected area [m$^2$] | 0.015 |
| Fixed drag coefficient [–] | 2.2 |
| HUMSAT-D mass (no Cube-de-ALPS) [kg] | 1 |
| Total mass (incl. Cube-de-ALPS) [kg] | 1.2 |

When using $\hat{T}_{eff}$ in the ODE integration of Eqs. (13), the thrusting cone half-angle $\alpha$ is updated as a function of current orbital altitude by re-arranging Eq. (4) for $A_{fc}(\alpha)$. We then invert Eq. (3) for $d$ using a numerical root solver. Finally, the trivial relationship between $d$ and $\alpha$ is given by Eq. (2).

As Eq. (3) is not invertible, there is no analytical expression for $\alpha$. To avoid using a numerical root solver at every step of the integration, we pre-compute values $\alpha$ for every 10 m between 150 km and 2000 km. We then linearly interpolate between the data points to update $\hat{T}_{eff}$ at every integrator step.

This change in $\alpha$ over time influences the fraction of time the system is thrusting, $\tau_t$, which also affects the average fuel consumption rate. To accurately track the remaining fuel on board, we use the total impulse delivered to estimate the fuel consumption and fire as long as we have not delivered all the onboard impulse. The ODE for the impulse delivered is expressed as

$$\dot{I}_{used}(t) = T_0 \tau_t(\alpha) \tag{28}$$

and is integrated alongside the modified equinoctial equations in (13). Therefore, the thrust value $T_{ODE}$ turns off when all onboard fuel has been consumed,

$$T_{ODE} = \begin{cases} \hat{T}_{eff}, & \text{if } \frac{I_{used}(t)}{I_0} \leq 1 \\ 0, & \text{otherwise} \end{cases} \tag{29}$$

where $I_0$ is the total onboard impulse.

## 4. System performance analysis

Using the semi-analytical propagator, we systematically analyse Cube-de-ALPS system parameters, including fuel material, layout, and signal-to-noise ratio, and their impact on the de-orbiting performance. To that end, we integrate Cube-de-ALPS into HUMSAT-D, with satellite characteristics outlined in Table 2. We assess silver, aluminium, tungsten and copper as fuel materials by changing the thrust level and the firing time, which are both material-dependent quantities [48]. The layout analysis distributes the thruster system across opposing faces to increase thrusting time while maintaining the total amount of fuel. Varying the signal-to-noise ratio changes the thrusting cone size and its behaviour with altitude, which leads to a change in de-orbiting performance.

We use the semi-analytical propagator introduced in Section 3 to limit the computational runtimes. The simulation stops when the spacecraft reaches 150 km. If the thruster stops firing at a higher altitude, atmospheric drag naturally decays the spacecraft. The satellite is given 90 simulated years to reach 150 km to avoid unnecessarily long computation times. If this time limit is reached, the simulation stops before re-entry occurs.

### 4.1. Cube-de-ALPS fuel material

First, we determine the best fuel material for Cube-de-ALPS by simulating its de-orbiting time from different initial altitudes. The fuels selected for analysis are the materials used in the physical prototypes of Cube-de-ALPS. The thruster system has been tested with a printed polymer composed of 87% of silver by weight, machined copper, and machined aluminium, respectively, as the propellant [23]. We also include tungsten in the comparison, as it is theoretically the propellant with the highest impulse that can be fitted on Cube-de-ALPS.

The thruster system has the maximum amount of each propellant while respecting the fuel mass and pixel size restrictions listed in Table 1. Table 3 summarises the propellant selected for testing and their respective properties.

We look at the de-orbiting time of the HUMSAT-D CubeSat between 150 km and 2000 km when equipped with Cube-de-ALPS. The results are shown in Fig. 5, where the curve labelled “no Cube-de-ALPS” corresponds to the simulated natural decay of HUMSAT-D at different altitudes. The non-linearities in the curves are due to the atmospheric density variation with respect to time. We define the maximum altitude of Cube-de-ALPS as the height above which the HUMSAT-D satellite would not de-orbit within 25 years. Therefore, the maximum altitude lies on the 25-year line.

At around 400 km, we identify the point where the benefits of the thrust from Cube-de-ALPS do not outweigh the drawback of the additional mass from the system. Therefore, the system is beneficial only for altitudes above this point until its maximum de-orbiting altitude.

The results also show that the silver propellant de-orbits faster initially due to its higher thrust, but its limited total impulse, due to pixel size restrictions, means its maximum altitude is lower than copper.

Even though tungsten outperforms all the other materials, we choose copper as fuel for the remainder of this work, as our simulations show it has the best de-orbiting performance of all the manufactured materials. We simulated the decay times for signal-to-noise ratios of 2, 3 and 4 and established that the choice of material is independent of the mode of operation.

### 4.2. Layout comparison

The 1-F and 2-F layouts are compared in this section by inspecting their de-orbiting performance. As shown through Eq. (27), splitting Cube-de-ALPS across two faces doubles the effective thrust, although the total impulse remains the same since both layouts have the same amount of fuel.

Fig. 6 shows the decay times for HUMSAT-D with the 1-F and 2-F configurations at different signal-to-noise ratios, which is discussed in Section 4.3. Due to its higher thrust, the 2-F layout performs better at lower altitudes, where the de-orbiting happens before the CubeSat has burnt out its fuel, i.e. it is still firing, and not all the impulse has been delivered. After the burnout point, represented on the graph as an inflection point, the curves for the 2-F layout rapidly converge towards their 1-F equivalent. At that point, both systems have delivered the same impulse against the velocity direction, and the high burnout altitude means the total de-orbiting time is dominated by natural decay, hence the similar de-orbiting performance. Fig. 6 also shows that this behaviour does not change for different signal-to-noise ratios.

Therefore, the preferred setup is the 2-F layout, which will provide faster de-orbiting for altitudes below its burnout point and similar performance to the 1-F beyond that height.

### 4.3. Signal-to-noise impact

Lastly, we investigate the effect of the signal-to-noise ratio on the decay times by varying $SN$ between 1 and 10. Fig. 6 shows the de-orbiting times of HUMSAT-D, using Cube-de-ALPS with copper, at different signal-to-noise ratios. Interestingly, we note that the signal-to-noise ratio that leads to the fastest de-orbiting is not constant but varies with altitude.

Low signal-to-noise ratios are favoured at lower orbital heights because they lead to a broader thrusting cone, which yields a higher effective thrust at the expense of total delivered impulse. As the initial

**Table 3**
Fuel materials for Cube-de-ALPS [48].

| Fuel | Nominal thrust [μN] | Firing time [days] | Pixel height [mm] | Fuel mass [g] |
|---|---|---|---|---|
| Silver (Ag) | 27.8 | 122.92 | 3.6 | 94 |
| Aluminium (Al) | 11.5 | 152.18 | 3.6 | 23 |
| Copper (Cu) | 17.6 | 416 | 3.6 | 80 |
| Tungsten (W) | 27.5 | 449.34 | 2.08 | 100 |

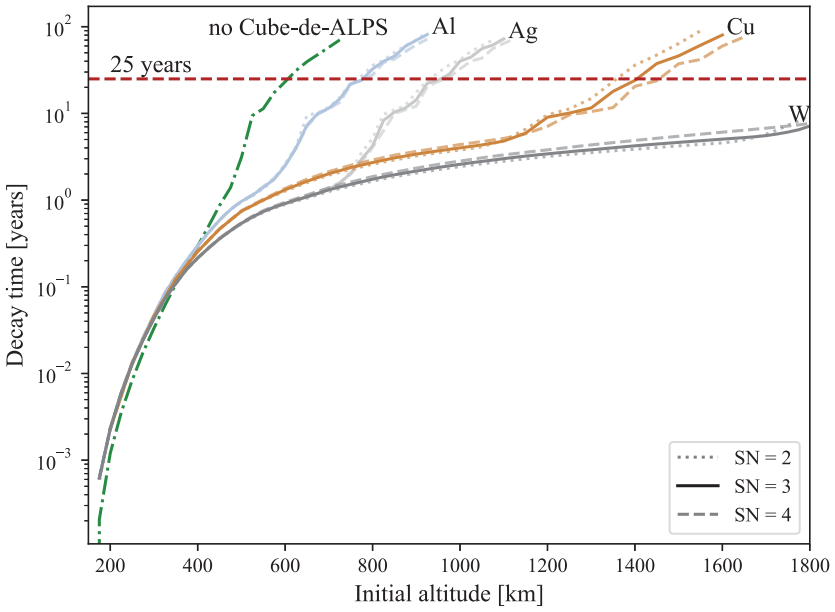


**Fig. 5.** Decay time with respect to altitude for Copper (Cu), aluminium (Al), Tungsten (W), and printed silver (Ag). The plot presents the semi-analytical results and a baseline, corresponding to HUMSAT-D naturally decaying without Cube-de-ALPS.

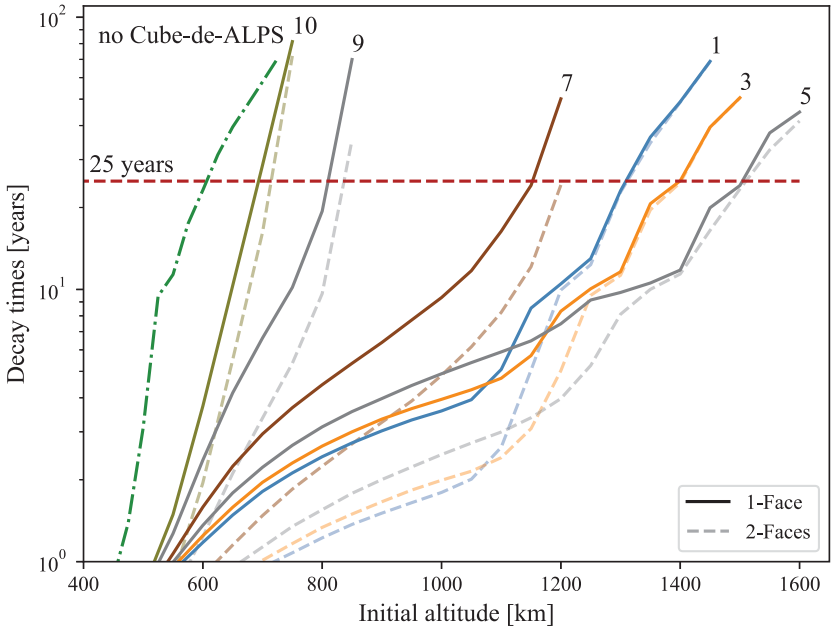


**Fig. 6.** Decay time with respect to altitude for Copper (Cu), using different signal-to-noise ratios for the 1-F and 2-F configurations.

altitude increases, the CubeSat requires more impulse to achieve de-orbiting, necessitating a smaller cone. Therefore, the signal-to-noise ratio leading to the quickest de-orbiting will be the lowest $SN$ providing the required impulse. However, a higher $SN$ also leads to less frequent firing, especially at higher altitudes, where strong signals are difficult to detect. As a result, Cube-de-ALPS practically never fires, leading the de-orbiting performance to worsen and approach the profile of natural decay. Such behaviour can be seen for the signal-to-noise ratios above 5, where the increased $SN$ pushes the curves towards the natural decay baseline.

The results described in this section allow us to define an operational zone for Cube-de-ALPS, as shown in Fig. 7. From Fig. 6, we

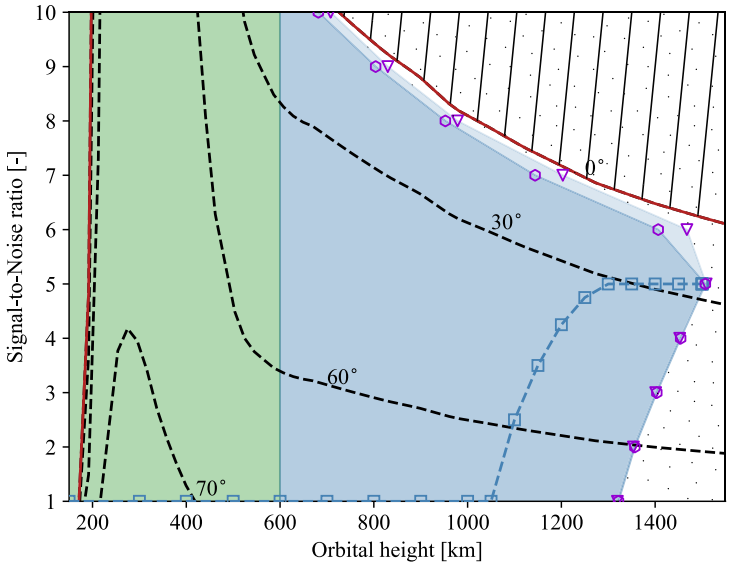


**Fig. 7.** Operational zone of Cube-de-ALPS. The green area ( ) highlights the altitudes for which HUMSAT-D would naturally decay. The blue shades define the zones where the 1-F ( ) and the 2-F ( ) can provide de-orbiting. The maximum altitude from which Cube-de-ALPS can provide de-orbiting is marked for the 1-F (▽) and the 2-F (○). For each initial altitude, the $SN$ leading to the fastest de-orbiting is also shown (—□—). The dotted area defines the heights and $SN$ where de-orbiting within 25 years is impossible, even with Cube-de-ALPS. Dashed contour lines (- - -) mark the maximum thrusting cone half-angle $\alpha$ detectable, with the red line (——) bounding a region where no cone is perceived. (For interpretation of the references to color in this figure legend, the reader is referred to the web version of this article.)

extract the maximum orbital height and the fastest $SN$ for each initial altitude. We highlight in blue the zone where Cube-de-ALPS allows de-orbiting, while the green area corresponds to the altitude where the CubeSat would naturally decay within 25 years.

The dashed contour lines correspond to the maximum half-cone angle detectable, the thrusting cone defined by $\alpha$. Therefore, the red line, denoting $\alpha = 0°$ corresponds to the boundary where no signal can be detected. In the hatched region beyond the red line, Cube-de-ALPS will never thrust, and the CubeSat will experience natural decay until it reaches an altitude where the detected signal is strong enough to trigger firing. This behaviour never leads to de-orbiting within 25 years in our simulations.

The best signal-to-noise ratio will vary based on the host spacecraft's mission and altitude, but ideally, the $SN$ that leads to the fastest decay should always be selected. If HUMSAT-D were equipped with Cube-de-ALPS, the recommended operational mode would be $SN = 1$.

## 5. High-fidelity numerical model

To validate our semi-analytical model used in the previous analysis, we increased the fidelity of our simulations by incorporating full attitude modelling into our propagator. This allows us to model the actual thrust direction instead of using the averaging method described in Section 3.5.

The attitude dynamics of the CubeSat and its interaction with the orbital motion are modelled using quaternion attitude kinematics [49,50]. We use the definition of a quaternion where the first three elements $q_1, q_2, q_3$ correspond to the vector part, and $q_4$ is a scalar. This quaternion encodes the rotation from the inertial to the body-fixed frame. The quaternion kinematics are expressed as

$$\dot{\vec{q}} = \frac{1}{2}\boldsymbol{\Lambda}\vec{q} \tag{30}$$

with

$$\boldsymbol{\Lambda} = \begin{pmatrix} 0 & \omega_z & -\omega_y & \omega_x \\ -\omega_z & 0 & \omega_x & \omega_y \\ \omega_y & -\omega_x & 0 & \omega_z \\ -\omega_x & -\omega_y & -\omega_z & 0 \end{pmatrix} \tag{31}$$

where $\omega_x$, $\omega_y$, $\omega_z$ are the components of the angular velocity vector expressed in the body-fixed frame.

The evolution of the angular velocity of an object is described by Euler's equation [51]

$$\dot{\vec{\omega}} = \mathbf{I}^{-1}(\vec{\tau}_{total} - \vec{\omega} \times \mathbf{I}\vec{\omega}) \tag{32}$$

where $\mathbf{I}$ is the satellite's inertia matrix, $\vec{\tau}_{total}$ is the torque applied, $\vec{\omega}$ is the angular velocity of the CubeSat, and $\dot{\vec{\omega}}$ is the angular acceleration. All parameters from Eq. (32) are expressed in the body-fixed frame. We integrate these equations along with the orbital ODE given in (13).

In addition to the attitude representation, higher fidelity is added to the thrust modelling. As mentioned in Section 2.1, the pulsed nature of the thrust leads the average to be closely distributed around the nominal thrust. We generate a random thrust according to a Gaussian distribution centred on the nominal thrust and with a standard deviation computed according to the Central Limit Theorem [25]. We model Cube-de-ALPS's grid of pixels in the simulator, allowing us to track the fuel consumption of each pixel individually and ensure that the thrust vector is attached to the pixel ignited. As most pixels do not align with the centre of mass of the CubeSat, the thrust, in addition to altering the orbital trajectory, will impart a torque on the CubeSat. We compute this torque with

$$\vec{\tau}_{thrust,i} = \vec{r}_{pixel,i} \times \vec{T} \tag{33}$$

where $\vec{r}_{pixel,i}$ is the position of the pixel that has ignited.

If the pixel selection is entirely random, the angular velocity of the CubeSat will rapidly increase, and the spacecraft will reach prohibitive spin rates [52]. Thus, we add a closed-loop thrusting law in the high-fidelity modelling, where Cube-de-ALPS will determine the quadrant in which a pixel can ignite. Based on angular velocity readings from its MEMS gyroscope, Cube-de-ALPS estimates the effect of firing each quadrant by assuming a pixel at each quadrant's centre will fire at the nominal thrust value. The system will select the quadrant that leads to the lowest final angular velocity.

Within the selected quadrant, one pixel will ignite based on the path of least electrical resistance within the circuit. For simplicity, we model all pixels within the selected quadrant with a uniform probability of being ignited.

The control law re-evaluates which quadrant to ignite every 100 s, unless Cube-de-ALPS leaves the thrusting cone. In this case, the control law re-assesses the quadrant when Cube-de-ALPS re-enters the thrusting cone.

We also add environmental torques to the propagator by modelling the spacecraft geometry read from an STL file. Force models that depend on the spacecraft geometry and orientation, such as solar radiation pressure, drag and lift, are applied to each facet of the spacecraft and produce both a force and torque on the satellite [50]. This provides an accurate, time-varying cross-section of the satellite, on top of modelling perturbations to the satellite's attitude.

## 6. Numerical results

This section presents the high-fidelity numerical results, validating the prior semi-analytical analysis. To adequately compare the results, the experimental setup used here is the same as discussed in Section 4.

Numerically propagating the attitude necessitates access to HUMSAT-D's inertia matrix. As this data was unavailable, we used the inertia matrix of SLUCUBE-2, a comparable 1U CubeSat [53]. We represent the added mass from Cube-de-ALPS by homogeneously increasing the inertia matrix by 20%,

$$\mathbf{I}_{HUMSAT-D} = \begin{pmatrix} 0.002184 & & \\ & 0.00222 & \\ & & 0.00264 \end{pmatrix} \text{ kg m}^2. \tag{34}$$

As the attitude is included, we specify that Cube-de-ALPS is mounted so that its normal is aligned with the body-fixed $x$-axis of the HUMSAT-D CubeSat. Cube-de-ALPS can thus provide torque around the satellite's y- and z- axes. Therefore the angle-of-attack $\theta$ is the angle between the body-fixed $x$-axis and the velocity direction,

$$\cos(\theta) = \hat{x} \cdot \hat{v}. \tag{35}$$

Due to the stochastic nature of quadrant selection and thrust generation, multiple realisations of each simulation are required. Preliminary trial runs indicate that 40 realisations per setup yield confidence intervals significantly smaller than the scale of the results, i.e. a decay time in years with a 95% confidence interval in weeks.

In the simulations, Cube-de-ALPS uses copper as fuel material and operates at a signal-to-noise ratio equal to 5. We choose $SN = 5$ to validate the maximum altitude from which Cube-de-ALPS can provide de-orbiting within 25 years. We impose a high initial angular velocity of 30 degrees per second on HUMSAT-D to simulate an out-of-control satellite. The complete numerical simulations continue until HUMSAT-D reaches 150 km, or Cube-de-ALPS has burnt out. In the latter case, should the CubeSat remain above the re-entry altitude of 150 km, the propagator deactivates the attitude propagation and only advances the orbit until 150 km is reached or 90 simulated years have elapsed. This transition allows for lower computational costs, as the complete numerical propagation involving attitude requires roughly 24 days for simulating approximately three years of active thrusting (mostly due to our non-optimised Python code).

We investigate the effect of the quadrant selection on HUMSAT-D and find that it successfully despins and maintains a low angular velocity throughout the simulations. Additionally, we compare the numerical decay times and the semi-analytical predictions, highlighting their resemblance and thus validating the work in Sections 3.5 and 4.

### 6.1. Angular velocity control

An example of the angular velocity profile with the closed-loop thrusting law is shown in Fig. 8. The CubeSat is given 30 degrees per second as initial angular speed, which Cube-de-ALPS successfully de-spins to simulate the recovery of an out-of-control satellite. The angular velocity remains below one rotation per minute, except at the end, where a velocity spike appears. This spike is due to the random pixel selection, which yields unequal fuel consumption across the grid and leaves pockets of pixels that do not balance each other out at the end, spinning up the satellite. As the spike appears only at the end of the firing time, operators can either ignore it, as Cube-de-ALPS will have de-orbited the spacecraft, or stop firing just before the angular velocity increases. On average, 97% of the fuel has been consumed before the velocity spike appears, which leads to minimal impact on the de-orbiting performance.

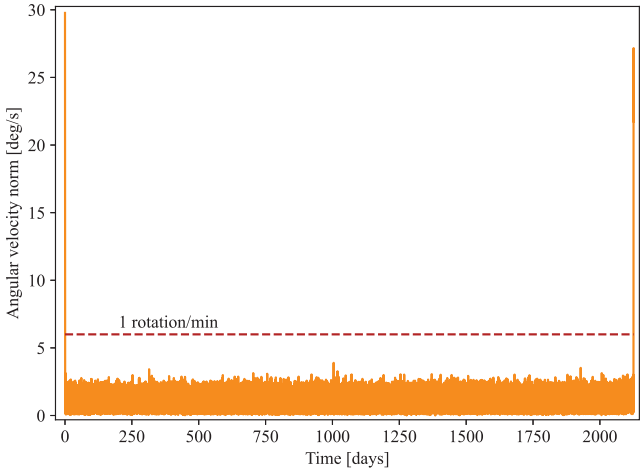


**Fig. 8.** Example of the angular velocity of a 1U CubeSat equipped with Cube-de-ALPS using the closed-loop control law.

During the velocity spike, the control law will attempt to control the satellite's y- and $z$-axis, while the coupling effect of the non-uniform distribution of mass will build momentum around the $x$-axis. This induces spin stabilisation around the axis that Cube-de-ALPS cannot control, which in turn affects the thrust delivery. If the satellite is stabilised with its thruster pointing far outside the orbital plane, the thrust delivery is diminished due to reduced firing opportunities and a lower thrust component against the velocity vector. The opposite is true for a satellite that has stabilised with its thruster close to the orbital plane. Therefore, the satellite's spin rate influences the system's performance, reinforcing the need for a control law to manage the angular velocity.

### 6.2. High-fidelity decommissioning times

Lastly, we simulate HUMSAT-D de-orbiting from various initial altitudes, using the high-fidelity environment. Both the 1-Face (1-F) and 2-Faces (2-F) layouts are analysed at a signal-to-noise ratio of 5. For each initial altitude, 40 realisations are run, allowing the construction of a confidence interval of 95%. Fig. 9 shows the high-fidelity decay times and compares them to the estimates obtained in Section 4, which match closely. Visible on the right of the graph, the convergence predicted by the estimates is confirmed by the high-fidelity results.

The consistency between the estimates and the predicted results shows that the assumptions made in the semi-analytical propagator in Section 3.5 are valid, and the subsequent results obtained in Section 4 are correct and Cube-de-ALPS will provide de-orbiting capacity from 1400 km within 25 years.

## 7. Conclusion

In this work, we have introduced Cube-de-ALPS, a fully printed standalone propulsion package that uses a gyroscope and a Faraday cup for attitude estimation. An operational mode was outlined, requiring only coarse angle-of-attack estimates and angular velocity readings.

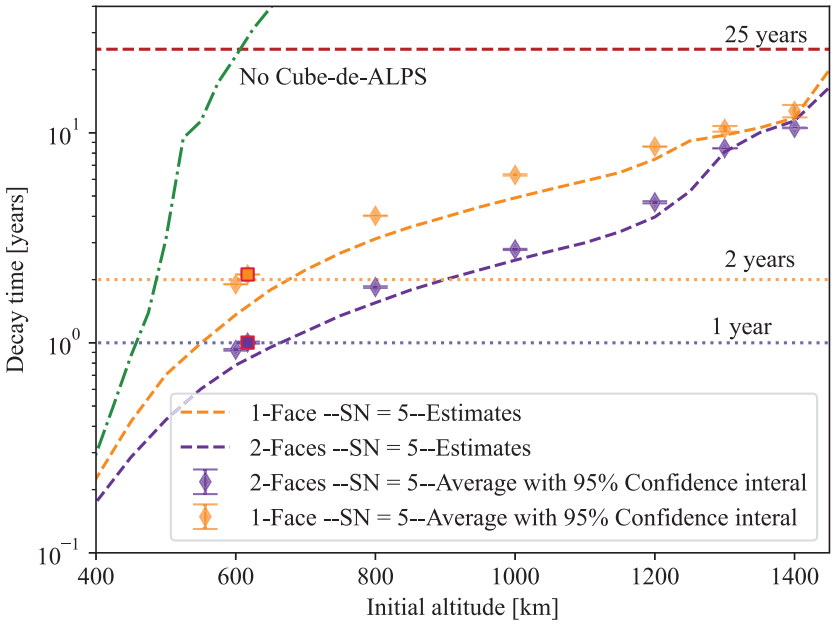


**Fig. 9.** High-fidelity numerical decay time predictions compared to the semi-analytical estimation. The altitude of the HUMSAT-D satellite is marked for the 1-F (■) and the 2-F (■) configurations.

We equipped Cube-de-ALPS on HUMSAT-D, a 1U CubeSat that spent seven years in LEO as an untracked space debris and simulated de-orbiting missions.

Using a semi-analytical model, the de-orbiting performance is investigated for different fuel materials, layouts, and signal-to-noise ratios. We used a high-fidelity numerical model, which includes full attitude propagation, to validate our results and show that Cube-de-ALPS would have decayed HUMSAT-D much faster than naturally possible.

In conclusion, Cube-de-ALPS can provide de-orbiting capacity as intended and will allow 1U CubeSats to operate up to 1400 km, more than twice as high as naturally possible, while ensuring re-entry within 25 years.

## Declaration of competing interest

The authors declare the following financial interests/personal relationships which may be considered as potential competing interests: The authors report financial support was provided by the European Space Agency. All authors declare that they have no known competing financial interests or personal relationships that could have appeared to influence the work reported in this paper.

## Acknowledgements

The authors acknowledge the use of the IRIDIS High-Performance Computing Facility and associated support services at the University of Southampton, in the completion of this work. This work was partially supported by the European Space Agency, France [grant 4000140067/22/NL/AL/mma].

## References

[1] A. Kramer, P. Bangert, K. Schilling, UWE-4: First electric propulsion on a 1U cubesat-in-orbit experiments and characterization, Aerospace 7 (7) (2020) http://dx.doi.org/10.3390/AEROSPACE7070098.

[2] K. Lemmer, Propulsion for CubeSats, Acta Astronaut. 134 (January) (2017) 231–243, http://dx.doi.org/10.1016/j.actaastro.2017.01.048.

[3] H.G. Lewis, B.S. Schwarz, S.G. George, H. Stokes, An Assessment of CubeSat Collision Risk, Tech. rep., 2014.

[4] SpaceWorks, Nano/Microsatellite Market Forecast, 10th, 2020.

[5] E. Kulu, Nanosat Database. URL https://www.nanosats.eu/.

[6] T. Villela, C.A. Costa, A.M. Brandão, F.T. Bueno, R. Leonardi, Towards the thousandth CubeSat: A statistical overview, Int. J. Aerosp. Eng. 2019 (2019) http://dx.doi.org/10.1155/2019/5063145.

[7] NASA, Process for Limiting Orbital Debris -NASA-STD-8719.14B, Tech. rep., 2007.

[8] D.L. Oltrogge, K. Leveque, An Evaluation of CubeSat Orbital Decay, in: 25th Annu. AIAA/USU Conf. Small Satell. (2011), 2011, pp. 0–12.

[9] N.M. Suhadis, Statistical Overview of Cubesat Mission, Springer Singapore, 2020, http://dx.doi.org/10.1007/978-981-15-4756-0{_}50, no. 2003.

[10] R. Munakata, Cubesat design specification rev. 13, in: CubeSat Program, Vol. 8651, Calif. Polytech. State, 2009, p. 22.

[11] R. Birkeland, CubeSat propulsion: Expanding the affordable space platform (january), 2018.

[12] J. Hudson, S. Spangelo, A. Hine, D. Kolosa, K. Lemmer, Mission analysis for CubeSats with micropropulsion, J. Spacecr. Rockets 53 (5) (2016) 836–846, http://dx.doi.org/10.2514/1.A33564.

[13] NASA, State - of - the - Art Small Spacecraft Technology (October), NASA/TP–2020–5008734, 2021.

[14] C. Clark, Clark SSC10-III-5 Huge Power Demand.Itsy-Bitsy Satellite: Solving the CubeSat Power Paradox, Tech. rep..

[15] SPACEMIND, SM-SP Datasheet, Tech. rep., 2020.

[16] A.R. Tummala, A. Dutta, An overview of cube-satellite propulsion technologies and trends, Aerospace 4 (4) (2017) 1–30, http://dx.doi.org/10.3390/aerospace4040058.

[17] I. Levchenko, K. Bazaka, Y. Ding, Y. Raitses, S. Mazouffre, T. Henning, P.J. Klar, S. Shinohara, J. Schein, L. Garrigues, M. Kim, D. Lev, F. Taccogna, R.W. Boswell, C. Charles, H. Koizumi, Y. Shen, C. Scharlemann, M. Keidar, S. Xu, Space micropropulsion systems for cubesats and small satellites: From proximate targets to furthermost frontiers, Appl. Phys. Rev. 5 (1) (2018) http://dx.doi.org/10.1063/1.5007734.

[18] G. Quinsac, B. Segret, C. Koppel, B. Mosser, Attitude control: A key factor during the design of low-thrust propulsion for CubeSats, Acta Astronaut. 176 (2020) 40–51, http://dx.doi.org/10.1016/j.actaastro.2020.03.053.

[19] S. Ciaralli, M. Coletti, S.B. Gabriel, Results of the qualification test campaign of a pulsed plasma thruster for cubesat propulsion (PPTCUP), Acta Astronaut. 121 (2016) 314–322, http://dx.doi.org/10.1016/j.actaastro.2015.08.016.

[20] M. Coletti, F. Guarducci, S.B. Gabriel, A micro PPT for cubesat application: Design and preliminary experimental results, Acta Astronaut. 69 (3–4) (2011) 200–208, http://dx.doi.org/10.1016/j.actaastro.2011.03.008.

[21] J.T. King, J. Kolbeck, J.S. Kang, M. Sanders, M. Keidar, Performance analysis of nano-sat scale $\mu$cat electric propulsion for 3U CubeSat attitude control, 2021, http://dx.doi.org/10.1016/j.actaastro.2020.10.006.

[22] J. Saletes, K. Saddul, M.K. Kim, A. Wittig, Innovative Propulsion Systems for CubeSats and MicroSats-EXPRO+: CubeSat de-Orbit ALl-Printed Propulsion System Final Report, Tech. rep., 2022.

[23] J. Saletes, M. Kim, K. Saddul, A. Wittig, K. Honda, P. Katila, Development of a Novel CubeSat de-Orbiting All Printed Propulsion System, Tech. rep., 2022.

[24] Camanzo-Mariño, Aguado-Agelet, González-Muiño, Pérez-Lissi, Vázquez, Fernández-Fernández, HUMSAT-d revival: Recovery operations and root cause analysis after 7 years of no contact, in: International Astronautical Congress Conference Proceedings, 2022-March, IEEE Computer Society, 2022, http://dx.doi.org/10.1109/AERO53065.2022.9843810.
[25] Peck Roxy, Olsen Chris, Devore Jay, Introduction To Statistics and Data Analysis, Tech. rep.
[26] SAFRAN, STIM277H Multi-Axis Gyro Module, Tech. rep.
[27] CubeSPACE, CubeADCS the Complete ADCS Solution Interface Control Document, Tech. rep.
[28] Y. Watanabe, K. Suzuki, K. Yamada, Attitude Estimation of Nano-Satellite with Deployable Aeroshell During Orbital Decay, Tech. Rep. ists30, 2016.
[29] N. Enoki, Y. Takahashi, N. Oshima, K. Yamada, K. Suzuki, Aerodynamics of inflatable nano-satellite eGG in low earth orbit and reentry duration, in: AIP Conference Proceedings, Vol. 2132, American Institute of Physics Inc., 2019, http://dx.doi.org/10.1063/1.5119597.
[30] B. Nanan, C.Y. Chen, J.Y. Liu, N. Balan, C.Y. Chen, G.J. Bailey, Behaviour of the Low-Latitude Ionosphere-Plasmasphere System At Long Deep Solar Minimum, Tech. rep., 2012.
[31] Lee H. Sentman, Free Molecule Flow Theory and Its Application To the Determination of Aerodynamic Forces, Lockheed Aircraft Corporation, 1961.
[32] E. Weisstein, Circle-Circle Intersection. URL https://mathworld.wolfram.com/Circle-CircleIntersection.html.
[33] W.R. Hoegy, J.M. Grebowsky, L.H. Brace, Ionospheric Ion Composition from Satellite Measurements Made During 1970-1980: Altitudes Profiles, Tech. Rep., Vol. 10, 1991.
[34] E.A. Rotii, The Gaussian Form of the Variation-of-Parameter Equations Formulated in Equinoctial Elements- Applications, Tech. Rep., Vol. 10, 1985.
[35] S. Frey, C. Colombo, S. Lemmens, Extension of the king-hele orbit contraction method for accurate, semi-analytical propagation of non-circular orbits, Adv. Sp. Res. 64 (1) (2019) 1–17, http://dx.doi.org/10.1016/j.asr.2019.03.016.
[36] D.A. Vallado, Fundamentals of Astrodynamics and Applications, Microcosm Press, 2013.
[37] N.K. Pavlis, S.A. Holmes, S.C. Kenyon, J.K. Factor, The development and evaluation of the earth gravitational model 2008 (EGM2008), J. Geophys. Res.: Solid Earth 117 (4) (2012) 1–38, http://dx.doi.org/10.1029/2011JB008916.
[38] A. Annex, B. Pearson, B. Seignovert, B. Carcich, H. Eichhorn, J. Mapel, J. von Forstner, J. McAuliffe, J. del Rio, K. Berry, K.-M. Aye, M. Stefko, M. de Val-Borro, S. Kulumani, S. y. Murakami, Spiceypy: a pythonic wrapper for the SPICE toolkit, J. Open Sour. Softw. 5 (46) (2020) 2050, http://dx.doi.org/10.21105/joss.02050.
[39] C.H. Acton, Ancillary Data Services of NASA's Navigation and Ancillary Information Facility, Tech. Rep., Vol. 1, 1996.
[40] C. Acton, N. Bachman, B. Semenov, E. Wright, A look towards the future in the handling of space science mission geometry, Planet. Space Sci. 150 (2018) 9–12, http://dx.doi.org/10.1016/j.pss.2017.02.013.
[41] O. Montenbruck, E. Gill, Satellite Orbits, Springer, 2000.
[42] General Mission Analysis Tool (GMAT) Mathematical Specifications, Tech. rep., NASA Goddard Space Flight Center, , 2020.
[43] R.S. Park, W.M. Folkner, J.G. Williams, D.H. Boggs, The JPL planetary and lunar ephemerides DE440 and DE441, Astron. J. 161 (3) (2021) 105, http://dx.doi.org/10.3847/1538-3881/abd414.
[44] H.C. Polat, J. Virgili-Llop, M. Romano, Statistical analysis and classification of launched CubeSat missions with emphasis on the attitude control method, JoSS 5 (3) (2016) 513–530.
[45] D.T. Gerhardt, S.E. Palo Advisor, Passive Magnetic Attitude Control for CubeSat Spacecraft, Tech. rep.
[46] M. Berthet, K. Suzuki, Coupled simulation of passive aerodynamic stabilisation of a nanosatellite during orbital decay, Trans. Japan Soc. Aeronaut. Space Sci. Aerosp. Technol. Japan 18 (6) (2020) 384–390, http://dx.doi.org/10.2322/tastj.18.384.
[47] A.D. Polyanin, A.V. Manzhirov, Handbook of Mathematics for Engineers and Scientists, Chapman and Hall/CRC, 2006, http://dx.doi.org/10.1201/9781420010510.
[48] J.E. Polk, M.J. Sekerak, J.K. Ziemer, J. Schein, N. Qi, A. Anders, A theoretical analysis of vacuum arc thruster and vacuum arc ion thruster performance, IEEE Trans. Plasma Sci. 36 (5 PART 1) (2008) 2167–2179, http://dx.doi.org/10.1109/TPS.2008.2004374.
[49] H. Curtis, Orbital Mechanics for Engineering Students, Elsevier, 2005.
[50] F. Landis Markley, J.L. Crassidis, Fundamentals of Spacecraft Attitude Determination and Control.
[51] Y. Yang, Spacecraft attitude determination and control: Quaternion based method, Annu. Rev. Control 36 (2) (2012) 198–219, http://dx.doi.org/10.1016/j.arcontrol.2012.09.003.
[52] K. Saddul, A. Wittig, J. Saletes, M. Kim, End-of-life disposal of sub-3U CubeSat with a printed thin-film vacuum arc thruster, in: Proceedings of the International Astronautical Congress, 2022.
[53] S. Jayaram, D. Pais, Model-based Simulation of Passive Attitude Control of SLUCUBE-2 Using Nonlinear Hysteresis and Geomagnetic Models, Int. J. Aerosp. Sci. 1 (4) (2012) 77–84, http://dx.doi.org/10.5923/j.aerospace.20120104.04.